COMPUTER-AIDED DIAGNOSTIC TOOL FOR EARLY DETECTION OF PROSTATE CANCER

Islam Reda[1,2], Ahmed Shalaby[2], Fahmi Khalifa[2], Mohammed Elmogy[1], Ahmed Aboulfotouh[1], Mohamed Abou El-Ghar[3], Ehsan Hosseini-Asl[4], Naoufel Werghi[5], Robert Keynton[2], and Ayman El-Baz[2*]

[1]Faculty of Computers and Information, Mansoura University, Mansoura 35516, Egypt.

[2]Bioengineering Department,University of Louisville, Louisville, KY, USA.

[3]Radiology Department, Urology and Nephrology Center, University of Mansoura, Mansoura 35516, Egypt.

[4]Electrical and Computer Engineering, University of Louisville, Louisville, KY, USA.

[5]Khalifa University of Science Technology and Research, Abu Dhabi, UAE.

ABSTRACT

In this paper, we propose a novel non-invasive framework for the early diagnosis of prostate cancer from diffusion-weighted magnetic resonance imaging (DW-MRI). The proposed approach consists of three main steps. In the first step, the prostate is localized and segmented based on a new level-set model. In the second step, the apparent diffusion coefficient (ADC) of the segmented prostate volume is mathematically calculated for different b-values. To preserve continuity, the calculated ADC values are normalized and refined using a Generalized Gauss-Markov Random Field (GGMRF) image model. The cumulative distribution function (CDF) of refined ADC for the prostate tissues at different b-values are then constructed. These CDFs are considered as global features describing water diffusion which can be used to distinguish between benign and malignant tumors. Finally, a deep learning auto-encoder network, trained by a stacked non-negativity constraint algorithm (SNCAE), is used to classify the prostate tumor as benign or malignant based on the CDFs extracted from the previous step. Preliminary experiments on 53 clinical DW-MRI data sets resulted in 100% correct classification, indicating the high accuracy of the proposed framework and holding promise of the proposed CAD system as a reliable non-invasive diagnostic tool.

Index Terms— Prostate cancer, NMF, MGRF, CAD

1. INTRODUCTION

Prostatic carcinoma is one of the major causes of cancer related deaths among men in the United States and the Western world with estimates of 220,800 new prostate cancer cases and about 27,540 deaths because of prostate cancer among Americans in 2015 [1]. Fortunately, the detection of prostatic carcinoma in its initial stages can enhance the survival rate. At present, the standard diagnostic technique is to perform a transrectal ultrasound (TRUS) guided needle biopsy after a positive prostate specific antigen (PSA) test result. When there is a disagreement between the PSA level and the results of TRUS guided biopsy (such as, elevated PSA level when the biopsy result is negative), the use of MRI to detect prostatic carcinoma can be significant [2].

In general, T2-weighted MRI has been the most popular MRI technique used for detecting prostatic carcinoma. The reported sensitivity using T2-weighted MRI alone is good but the associated specificity is low [3]. Recently, the trend is to use functional MRI modalities such as dynamic contrast-enhanced (DCE)-MRI and DW-MRI to improve the diagnostic accuracy. DCE-MRI has been extensively used in several applications [4–11], in addition to detection of prostate cancer [12–15]. DCE-MRI depends on contrast agents (e.g., gadolinium) to enhance the contrast between the different tissue types and make the visualization of the anatomical structures easier. However, DCE-MR images require long acquisition time and contrast agents are harmful especially for patients with kidney problems. On the other hand, DW-MRI measures the sensitivity of tissues to the water molecule motion by applying pairs of opposing magnetic field gradients. Although the resolution of DW-MR images is lower than DCE-MR images, DW-MR images have distinct advantages over DCE-MR images as they can be acquired very quickly, without the use of contrast agents or special hardware [16]. Comparing DW-MRI with T2-weighted MRI or DCE-MRI showed that the diagnostic accuracy of DW-MRI is better than each of the other two modalities [17].

A small number of prostate cancer CAD systems have evaluated the use of DW-MR images alone or in combination with other MRI modalities. For instance, a DW-MRI based CAD system was developed by Firjani et al. [18] that utilized three intensity features and a K-nearest neighbors (KNN) classifier to distinguish between benign and malignant cases. The first multiparametric CAD system was proposed by Chan et al. [19] using T2-MRI, T2-mapping, and line scan diffusion imaging (LSDI). In their system, intensity and textural features were extracted from manually-outlined ROI and fed into two different classifiers: support vector machine (SVM) and Fisher linear discriminant (FLD) classifiers to detect the presence of prostate cancer in the peripheral zone (PZ) of the prostate. The area under the curve (AUC) for the two classifiers were 0.761 ± 0.043 and 0.839 ± 0.064, respectively. Another multiparametric CAD system for detecting prostate cancer in the PZ of the prostate was developed by Niaf et al. [20]. Their system used a feature set derived from T2-weighted MRI, DCE-MRI, and DW-MRI to train and compare four different classifiers: KNN, linear discriminant analysis (LDA), naive Bayes, and nonlinear SVM. The same three MRI modalities used by the previous system were used in the CAD system presented by Vos et al. [21]. The prostate segmentation was done using the technique developed by Litjens et al. [22]. A combination of features (e.g., texture-based, ADC maps) was used by an LDA classifier to determine malignant and benign regions. In this paper, we develop a DW-MRI based CAD system for early detection of prostate cancer. Details and quantitative evaluation of the proposed system will be discussed in the following sections.

*Corresponding author:- Tel:(502)-852-5092, Fax:(502)-852-6806, E-mail: aselba01@exchange.louisville.edu

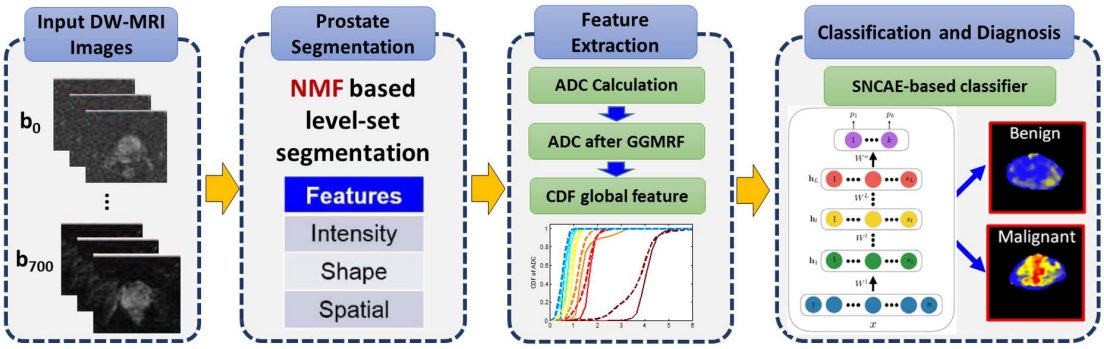

Fig. 1. Framework of the DW-MRI CAD system for early diagnosis of prostate cancer.

2. METHODOLOGY

In this paper, we develop a new automated non-invasive framework for early diagnosis of prostate cancer from DW-MRI. Fig. 1 summarizes the main steps of the proposed framework. It performs sequentially three steps. First, we implemented a segmentation method of the prostate tissues using our previously developed geometric deformable model (level-sets method) as described in [23]. This model is guided by a stochastic speed function that is derived using non-negative matrix factorization (NMF).The NMF attributes are calculated using information from the MRI intensity, a probabilistic shape model, and the spatial interactions between prostate voxels. The proposed method reaches 86.9% overall Dice similarity coefficient (DSC) and outperforms all other alternatives. For more details on this method and the comparison with other segmentation approaches, please see [23]. Afterwards, a global feature describing the water diffusion inside the prostate tissue is extracted based on ADC-CDFs. Finally, a deep learning auto-encoder network is used to classify the prostate tumor as benign or malignant based on the CDFs extracted from the previous step. The latter two steps of the proposed CAD system are discussed in detail in the following sections.

2.1. Global Feature Extraction

After the prostate tissues are segmented, discriminatory features are estimated from the segmented DW-MRI data and are used to distinguish between benign and malignant cases. In this paper, we used the apparent diffusion coefficient (ADC) as a discriminator feature to assess the tumor status, where the malignant tissues show a lower ADC at different b-values compared with benign and normal tissue due to the replacement of normal tissue [24]. To preserve continuity, the calculated ADC values are refined using a Generalized Gauss-Markov Random Field (GGMRF) image model with a 26-voxel neighborhood (Fig. 2). Continuity of the constructed 3-D volume is amplified by using their maximum a posteriori (MAP) estimates. In order to reduce data dimensionality, the cumulative distribution function (CDF) of the normalized ADC for the prostate tissues of each subject are estimated. These CDFs are considered as global features distinguishing between benign and malignant cases. Instead of using the whole 3D ADC, the resultant CDFs are used to train a stacked nonnegativity constraint autoencoder (SNCAE) classifier using the deep learning approach. The training sets contain 53 cases (27 benign and 26 malignant). Fig. 3 demonstrates examples for the average CDF of the 53 cases (the dotted red line is for benign cases and the solid blue line is for malignant cases) at different b-values: 100, 200, 300, 400, 500 and 700 s/mm^2, respectively. It is clear that the maximum difference and the largest separation between the benign and malignant subjects are shown at fig. 3 (f). Therefore, in the classification step, we expect that the most discriminatory feature between these two classes will be the CDF at b-value = 700 s/mm^2. More details and experiments will address this issue in the results section.

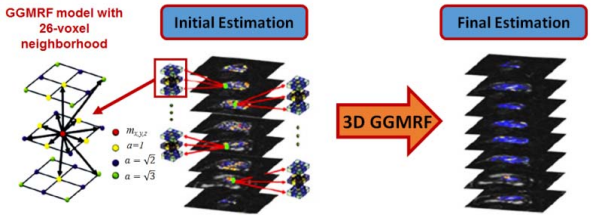

Fig. 2. Enhanced diffusion estimation and continuity analysis using the 3D GGMRF image model.

2.2. Stacked NCAE (SNCAE) Classifier

To classify the prostate tumor, our CAD system employs a deep neural network with a stack of autoencoders (AE) before the output layer that computes a softmax regression, generalizing the common logistic regression to more than two classes. Each AE compresses its input data to capture the most prominent variations and is built separately by greedy unsupervised pre-training [25]. The softmax output layer facilitates the subsequent supervised back-propagation-based fine tuning of the entire classifier by minimizing the total loss (negative log-likelihood) for given training labeled data. Using the AEs with a non-negativity constraint (NCAE) [26] yields both more reasonable data codes (features) during its unsupervised pre-training and better classification performance after the supervised refinement.

Let $\mathbf{W} = \{\mathbf{W}_j^{\mathrm{e}}, \mathbf{W}_i^{\mathrm{d}} : j = 1, \ldots, s;\ i = 1, \ldots, n\}$ denote a set of column vectors of weights for encoding (e) and decoding (d) layers of a single AE in Fig. 4. Let T denote vector transposition. The AE converts an n-dimensional column vector $\mathbf{u} = [u_1, \ldots, u_n]^{\mathsf{T}}$ of input signals into an s-dimensional column vector $\mathbf{h} = [h_1, \ldots, h_s]^{\mathsf{T}}$ of hidden codes (features, or activations), such that $s \ll n$, by uniform nonlinear transformation of s weighted linear combinations of signals:

$$h_j = \sigma\left(\left(\mathbf{W}_j^{\mathrm{e}}\right)^{\mathsf{T}}\mathbf{u}\right) \equiv \sigma\left(\sum_{i=1}^{n} w_{j:i}^{\mathrm{e}} u_i\right)$$

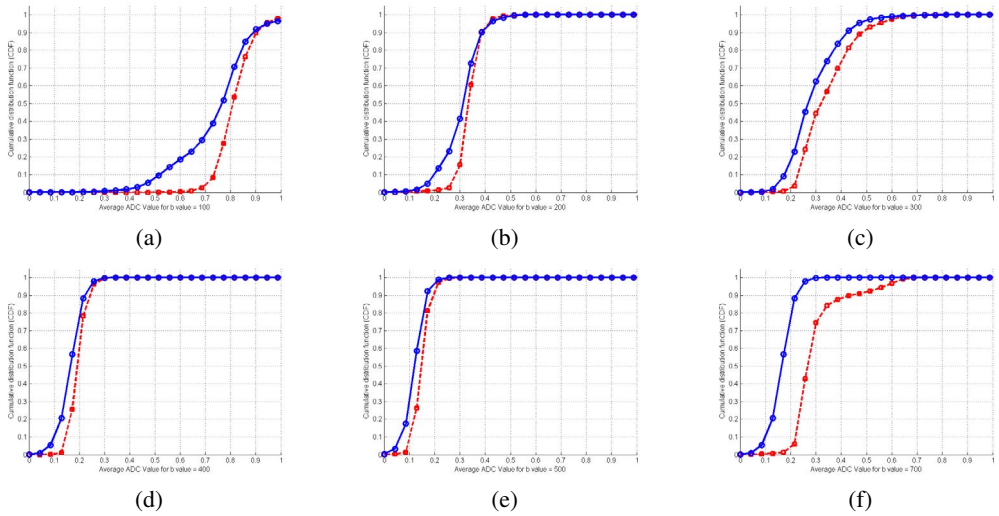

Fig. 3. The average CDF of the 53 cases (Benign: 27 cases and dotted red, Malignant: 26 cases and solid blue) at different b-values (a) b-value = 100 s/mm^2 (b) b-value = 200 s/mm^2, (c) b-value = 300 s/mm^2, (d) b-value = 400 s/mm^2, (e) b-value = 500 s/mm^2, and (f) b-value = 700 s/mm^2

where $\sigma(\ldots)$ is a certain sigmoid, i.e., a differentiable monotone scalar function with values in the range $[0, 1]$. Unsupervised pre-training of the AE minimizes total deviations between each given training input vector $\mathbf{u}_k$; $k = 1, \ldots, K$, and the same-dimensional vector, $\widehat{\mathbf{u}}_{\mathbf{W}:k}$ reconstructed from its code, or activation vector, $\mathbf{h}_k$. The total reconstruction error of applying such AE to compress and decompress the K training input vectors integrates the ℓ_2-norms of the deviations:

$$J_{\mathrm{AE}}(\mathbf{W}) = \frac{1}{2K} \sum_{k=1}^{K} \parallel \widehat{\mathbf{u}}_{\mathbf{W}:k} - \mathbf{u}_k \parallel^2 \tag{1}$$

To reduce the number of negative weights and enforce sparsity of the NCAE, the reconstruction error of Eq. (1) is appended, respectively, with quadratic negative weight penalties, $f(w_i) = (\min\{0, w_i\})^2$; $i = 1, \ldots, n$, and Kullback-Leibler (KL) divergence, $J_{\mathrm{KL}}(\mathbf{h}_{\mathbf{W}^{\mathrm{e}}}; \gamma)$, of activations, $\mathbf{h}_{\mathbf{W}^{\mathrm{e}}}$, obtained with the encoding weights $\mathbf{W}^{\mathrm{e}}$ for the training data, from a fixed small positive average value, γ, near 0:

$$\begin{aligned} J_{\mathrm{NCAE}}(\mathbf{W}) = J_{\mathrm{AE}}(\mathbf{W}) + \alpha \sum_{j=1}^{s} \sum_{i=1}^{n} f(w_{j:i}) \\ + \beta J_{\mathrm{KL}}(\mathbf{h}_{\mathbf{W}^{\mathrm{e}}}; \gamma) \end{aligned} \tag{2}$$

Here, the factors $\alpha \geq 0$ and $\beta \geq 0$ specify relative contributions of the non-negativity and sparsity constraints to the overall loss, $J_{\mathrm{NCAE}}(\mathbf{W})$, and

$$\begin{aligned} J_{\mathrm{KL}}(\mathbf{h}_{\mathbf{W}^{\mathrm{e}}}, \gamma) = \sum_{j=1}^{s} h_{\mathbf{W}^{\mathrm{e}}:j} \log \left(\frac{h_{\mathbf{W}^{\mathrm{e}}:j}}{\gamma} \right) \\ + (1 - h_{\mathbf{W}^{\mathrm{e}}:j}) \log \left(\frac{1 - h_{\mathbf{W}^{\mathrm{e}}:j}}{1 - \gamma} \right) \end{aligned} \tag{3}$$

The classifier is built by stacking the NCAE layers with an output softmax layer, as shown in Fig. 4. Each NCAE is pre-trained separately in the unsupervised mode, by using the activation vector of a lower layer as the input to the upper layer. In our case, the initial input data consisted of the 100-component CDFs, each of size 100. The bottom NCAE compresses the input vector to $s_1 = 50$ first-level activators, compressed by the next NCAE to $s_2 = 5$ second-level activators, which are reduced in turn by the output softmax layer to $s^{\circ} = 2$ values.

Separate pre-training of the first and second layers by minimizing the loss of Eq. (2) reduces the total reconstruction error, as well as increases sparsity of the extracted activations and numbers of the non-negative weights. The activations of the second NCAE layer, $\mathbf{h}^{[2]} = \sigma(\mathbf{W}_{[2]}^{\mathrm{e}\,\mathsf{T}} \mathbf{h}^{[1]})$, are inputs of the softmax classification layer, as sketched in Fig. 4 to compute a plausibility of a decision in favor of each particular output class, $c = 1, 2$:

$$p(c; \mathbf{W}_{\circ:c}) = \frac{\exp(\mathbf{W}_{\circ:c}^{\mathsf{T}} \mathbf{h}^{[2]})}{\exp(\mathbf{W}_{\circ:1}^{\mathsf{T}} \mathbf{h}^{[2]}) + \exp(\mathbf{W}_{\circ:2}^{\mathsf{T}} \mathbf{h}^{[2]})};$$

$$c = 1, 2; \ \sum_{c=1}^{2} p(c; \mathbf{W}_{\circ:c}; \mathbf{h}^{[2]}) = 1.$$

Its separate pre-training minimizes the total negative log-likelihood $J_{\circ}(\mathbf{W}_{\circ})$ of the known training classes, appended with the negative weight penalties:

$$J_{\circ}(\mathbf{W}^{o}) = -\frac{1}{K} \sum_{k=1}^{K} \log p(c_k; \mathbf{W}_{\circ:c}) + \alpha \sum_{c=1}^{2} \sum_{j=1}^{s_2} w_{\circ:c:j} \tag{4}$$

Finally, the entire stacked NCAE classifier (SNCAE) is fine-tuned on the labeled training data by the conventional error back-propagation through the network and penalizing only the negative weights of the softmax layer. In our experiments, $\alpha = 0.03$, $\beta = 3$, and $\gamma = 0.1$.

3. EXPERIMENTAL RESULTS

Experiments were conducted on 53 DW-MRI data sets that were obtained using a body coil Signa Horizon GE scanner in axial plane

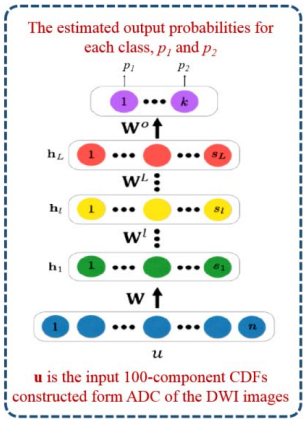

Fig. 4. Schematic diagram of a SNCAE classifier.

with the following parameters: Magnetic field strength: 1.5 Tesla; TE: 84.6 ms; TR: 8000 ms; Bandwidth: 142.86 khz; FOV: 34 cm^2; Slice thickness: 3 mm; Inter-slice gap: 0 mm; Acquisition sequence: conventional EPI; Diffusion weighting directions: mono direction; the used range of b values is from 0 to 700 s/mm^2. On average, 26 slices were obtained in 120 seconds to cover the prostate in each patient with voxel size of $1.25 \times 1.25 \times 3.00$ mm^3. All the subjects were diagnosed using a biopsy. The ground truths are performed on a slice-by-slice basis and obtained by manual segmentation using $Slicer^{©}$ (www.slicer.org). All annotations are verified by an expert.

To learn the statistical characteristics of both benign and malignant subjects, we trained our classifier by 53 DW-MRI datasets (27 benign and 26 malignant). The features involved for classification are the CDF of the normalized ADC maps for 7 different b-values of the segmented prostate tissue as shown in fig. 3. To assess the accuracy of our system, we perform a leave-one-out cross-validation test with the whole 53 datasets. We tried many scenarios to choose the optimum b-value (or values) for the best classification results. After many trials and combinations, we reach the following result: Among all available b-values, the b-value = 700 s/mm^2 is optimal. It outperforms all other available b-values. Moreover, it is better than using all b-values combined together. In other words, training our classifier using only b-value = 700 s/mm^2 gives us a better classification result than taking the majority voting of all 7 b-values results. The overall diagnostic accuracy for different b-values are summarized in Fig. 5. It is clear that b-value = 700 s/mm^2 has the highest accuracy results. And, this is coincided with what we get in fig. 3 (f).

To highlight the merit of using SNCAE-based classifier, a comparison between our classifier and four other ready-to-use classifiers (K*, K-nearest neighbor, Random Forest and Random Tree classifiers implemented in Weka toolbox) [27] is summarized in Table 1. As demonstrated in this table and using b-value = 700 s/mm^2 only, our classifier achieves an overall accuracy of 100% for all testing data sets. Also, the proposed framework outperforms the other alternatives and holds promise of the proposed CAD system as a reliable non-invasive diagnostic tool.

Additionally, we plot the receiver operating characteristics (ROC) curve for the developed CAD system and other classifiers to test the performance of our diagnostic tool. The results are demonstrated in fig. 6. As shown in this figure, the ROC area of the proposed classifier is the maximum and approaches 1 in comparison to other alternative.

Table 1. Classification accuracy, sensitivity, and specificity, for our CAD system and different classifiers from Weka tool.

Classifier	Accuracy	Sensitivity	Specificity
SNCAE (Proposed)	100%	100%	100%
K* (K-Star)	94.3%	94.3%	94.4%
KNN-Classifier (IBK)	88.67%	88.6%	88.7%
Random Forest	86.7%	86.8%	86.8%
Random Tree	84.9%	85.1%	84.9%

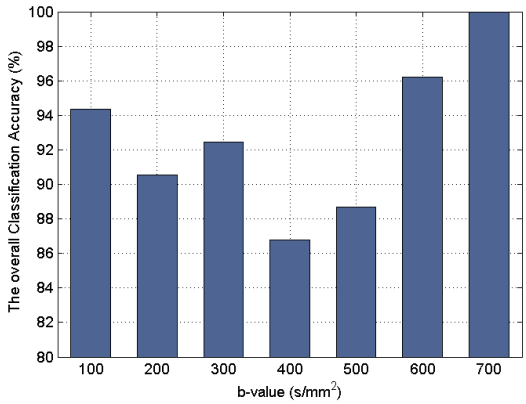

Fig. 5. Classification accuracy of SNCAE classifier using DWI datasets with different b-values.

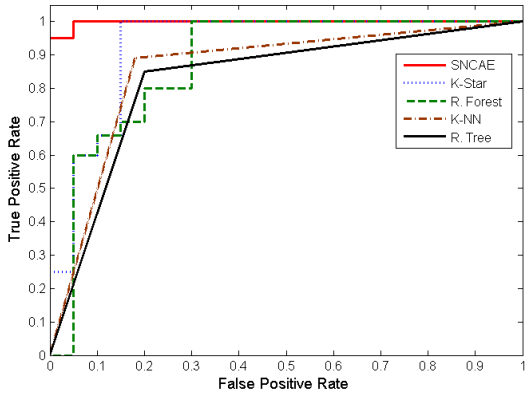

Fig. 6. The ROC curve for different classifiers. It is clear that, the SNCAE (proposed) outperforms all other alternative .

4. CONCLUSIONS

In this paper, we presented an image based computer aided diagnosis (CAD) system for early detection of prostate cancer using DW-MRI. The framework includes NMF based segmentation, diffusion parameters estimation (CDFs of the ADC), and SNCAE deep network based classification. We tested our CAD on 53 subjects with different b-values from 100 s/mm^2 to 700 s/mm^2. The experiments resulted in a 100% overall diagnostic accuracy when we trained our classifier using b-value = 700 s/mm^2 only. Applications of the proposed approach yield promising results that could, in the near future, replace the use of current technologies to determine the type of prostate cancer. **In future, we intend to increase the training and the testing datasets to confirm the accuracy and robustness of the proposed CAD system**.

5. REFERENCES

[1] R. L. Siegel, K. D. Miller, and A. Jemal, "Cancer statistics, 2015," *CA: a cancer journal for clinicians*, vol. 65, no. 1, pp. 5–29, 2015.

[2] N. Lawrentschuk and N. Fleshner, "The role of magnetic resonance imaging in targeting prostate cancer in patients with previous negative biopsies and elevated prostate-specific antigen levels," *BJU international*, vol. 103, no. 6, pp. 730–733, 2009.

[3] C. M. Hoeks, J. O. Barentsz, T. Hambrock, D. Yakar, D. M. Somford, S. W. Heijmink, T. W. Scheenen, P. C. Vos, H. Huisman, I. M. van Oort, et al., "Prostate cancer: multiparametric MR imaging for detection, localization, and staging," *Radiology*, vol. 261, no. 1, pp. 46–66, 2011.

[4] A. Farag, A. El-Baz, S. E. Yuksel, M. El-Ghar, and T. Eldiasty, "A framework for the detection of acute renal rejection with dynamic contrast enhanced magnetic resonance imaging," in *Proceedings of the 3rd IEEE International Symposium on Biomedical Imaging: From Nano to Macro, (ISBI'06)*, Arlington, VA, USA, April 6–9, 2006, IEEE, pp. 418–421.

[5] A. El-Baz, A. Farag, R. Fahmi, S. Yuksela, M. El-Ghar, and T. Eldiasty, "Image analysis of renal DCE MRI for the detection of acute renal rejection," in *Proceedings of the 18th International Conference on Pattern Recognition, (ICPR'06)*, Hong Kong, August 20–24, 2006, IEEE, vol. 3, pp. 822–825.

[6] A. El-Baz, A. A. Farag, S. E. Yuksel, M. E. El-Ghar, T. A. Eldiasty, and M. A. Ghoneim, "Application of deformable models for the detection of acute renal rejection," in *Deformable models*, pp. 293–333. Springer, 2007.

[7] A. El-Baz, G. Gimelfarb, and M. A. El-Ghar, "New motion correction models for automatic identification of renal transplant rejection," in *Medical Image Computing and Computer-Assisted Intervention–MICCAI 2007*, pp. 235–243. Springer, 2007.

[8] A. El-Baz, G. Gimel'farb, and M. El-Ghar, "A novel image analysis approach for accurate identification of acute renal rejection," in *Image Processing, 2008. ICIP 2008. 15th IEEE International Conference on*. IEEE, 2008, pp. 1812–1815.

[9] A. El-Baz, G. G. Farb, and M. El-Ghar, "Image analysis approach for identification of renal transplant rejection," in *Pattern Recognition, 2008. ICPR 2008. 19th International Conference on*. IEEE, 2008, pp. 1–4.

[10] F. Khalifa, A. El-Baz, G. Gimelfarb, and M. A. El-Ghar, "Non-invasive image-based approach for early detection of acute renal rejection," in *Medical Image Computing and Computer-Assisted Intervention–MICCAI 2010*, pp. 10–18. Springer, 2010.

[11] F. Khalifa, G. M. Beache, G. Gimel'farb, and A. El-Baz, "A novel CAD system for analyzing cardiac first-pass MR images," in *Pattern Recognition (ICPR), 2012 21st International Conference on*. IEEE, 2012, pp. 77–80.

[12] A. Firjani et al., "Non-invasive image-based approach for early detection of prostate cancer," in *Developments in E-systems Engineering (DeSE), 2011*. IEEE, 2011, pp. 172–177.

[13] A. Firjani et al., "A novel image-based approach for early detection of prostate cancer," in *Image Processing (ICIP), 2012 19th IEEE International Conference on*. IEEE, 2012, pp. 2849–2852.

[14] A. Firjani, F. Khalifa, A. Elnakib, G. Gimel'farb, M. A. El-Ghar, A. Elmaghraby, and A. El-Baz, "A novel image-based approach for early detection of prostate cancer using DCE-MRI," in *Computational Intelligence in Biomedical Imaging*, pp. 55–82. Springer, 2014.

[15] I. Reda et al., "A new NMF-autoencoder based cad system for early diagnosis of prostate cancer," in *Proceedings of the 13th IEEE International Symposium on Biomedical Imaging: From Nano to Macro, (ISBI'16)*, Prague, Czech Republic, April 13–16, 2016, IEEE, pp. 1237–1240.

[16] C. H. Tan, J. Wang, and V. Kundra, "Diffusion weighted imaging in prostate cancer," *European radiology*, vol. 21, no. 3, pp. 593–603, 2011.

[17] T. Tamada, T. Sone, Y. Jo, A. Yamamoto, and K. Ito, "Diffusion-weighted MRI and its role in prostate cancer," *NMR in Biomedicine*, vol. 27, no. 1, pp. 25–38, 2014.

[18] A. Firjani, A. Elnakib, F. Khalifa, G. Gimelfarb, M. A. El-Ghar, A. Elmaghraby, and A. El-Baz, "A diffusion-weighted imaging based diagnostic system for early detection of prostate cancer," *Journal of Biomedical Science and Engineering*, vol. 6, no. 03, pp. 346, 2013.

[19] I. Chan, W. Wells III, R. V. Mulkern, S. Haker, J. Zhang, K. H. Zou, S. E. Maier, and C. M. Tempany, "Detection of prostate cancer by integration of line-scan diffusion, T2-mapping and T2-weighted magnetic resonance imaging; a multichannel statistical classifier," *Medical Physics*, vol. 30, no. 9, pp. 2390–2398, 2003.

[20] E. Niaf, O. Rouvière, F. Mège-Lechevallier, F. Bratan, and C. Lartizien, "Computer-aided diagnosis of prostate cancer in the peripheral zone using multiparametric MRI," *Physics in Medicine and Biology*, vol. 57, no. 12, pp. 3833, 2012.

[21] P. Vos, J. Barentsz, N. Karssemeijer, and H. Huisman, "Automatic computer-aided detection of prostate cancer based on multiparametric magnetic resonance image analysis," *Physics in Medicine and Biology*, vol. 57, no. 6, pp. 1527, 2012.

[22] G. Litjens, P. Vos, J. Barentsz, N. Karssemeijer, and H. Huisman, "Automatic computer aided detection of abnormalities in multi-parametric prostate MRI," in *SPIE Medical Imaging*. International Society for Optics and Photonics, 2011, pp. 79630T–79630T.

[23] P. McClure, F. Khalifa, A. Soliman, M. A. El-Ghar, G. Gimelfarb, A. Elmagraby, and A. El-Baz, "A novel NMF guided level-set for DWI prostate segmentation," *J Comput Sci Syst Biol*, vol. 7, pp. 209–216, 2014.

[24] D. Le Bihan, "Apparent diffusion coefficient and beyond: what diffusion MR imaging can tell us about tissue structure," *Radiology*, vol. 268, no. 2, pp. 318–322, 2013.

[25] Y. Bengio, P. Lamblin, D. Popovici, and H. Larochelle, "Greedy layer-wise training of deep networks," *Advances in neural information processing systems*, vol. 19, pp. 153, 2007.

[26] E. Hosseini-Asl, J. Zurada, and O. Nasraoui, "Deep learning of part-based representation of data using sparse autoencoders with nonnegativity constraints," in *IEEE transactions on neural networks and learning systems*, 2015, vol. 99, pp. 1–13.

[27] M. Hall et al., "Hall, mark and frank, eibe and holmes, geoffrey and pfahringer, bernhard and reutemann, peter and witten, ian h," *ACM SIGKDD explorations newsletter*, vol. 11, no. 1, pp. 10–18, 2009.